This is a repository copy of *Lithiation phase behaviors of metal oxide anodes and extra capacities*.

White Rose Research Online URL for this paper:
https://eprints.whiterose.ac.uk/180854/

Version: Published Version

Article

# Lithiation phase behaviors of metal oxide anodes and extra capacities

Xiao Hua, Phoebe K. Allan, Harry S. Geddes, ..., Arianna Minelli, Peter G. Bruce, Andrew L. Goodwin

xiaohua716@gmail.com

### Highlights

The extra capacity may have a dominant source depending on specific metal species

$bcc$-FeO$_x$ intermediate lithiate via oxygen extraction from the Fe sublattice

Local structure characterization using pair distribution function

Robust phase deconvolution using Metropolis non-negative matrix factorization

Binary metal oxide anodes in lithium-ion batteries show extra capacities at their initial discharge. In this article, Hua et al. perform a systematic study of iron and manganese oxides' lithiation phase behaviors and report unexpected observations of $bcc$-FeO$_x$ solid solution and MnO pulverization, processes correlated with the extra capacities seen at different depths of discharge.

# Lithiation phase behaviors of metal oxide anodes and extra capacities

Xiao Hua,[1,7,8,*] Phoebe K. Allan,[2] Harry S. Geddes,[1] Elizabeth Castillo-Martínez,[3] Philip A. Chater,[4] Thomas S. Dean,[1] Arianna Minelli,[1] Peter G. Bruce,[5,6] and Andrew L. Goodwin[1]

## SUMMARY

**Binary metal oxides have received sustained interest as anode materials due to their desirable capacities, exceeding theoretical values particularly in the first discharge. Although they have received increasing attention in recent years, topical debates persist regarding not only their lithiation mechanisms but also the origin of additional capacity. Aiming to resolve these disagreements, we perform a systematic study of a series of iron and manganese oxides to investigate their phase behavior during first discharge. Using a combination of *in operando* pair distribution function measurements and our recently developed Metropolis non-negative matrix factorization approach to address the analytical challenges concerning materials' nanoscopic nature and phase heterogeneity, here we report unexpected observation of non-equilibrium $FeO_x$ solid-solution phases and pulverization of MnO. These processes are correlated with the extra capacities observed at different depths of discharge, pointing to a metal-dependent nature of this additional capacity and demonstrating the advantage of our approach with promising prospects for diverse applications.**

## INTRODUCTION

In the search for next-generation electrode materials for lithium-ion batteries (LIBs), there is often a tendency to focus on discovering new materials or morphologies. However, to be market friendly, these new technologies must be scalable.[1] An alternative strategy is to seek to resolve problems associated with longer-established, commercially attractive candidates. Binary (first-row transition) metal oxides ($M_xO_y$) are one such family. They are known as desirable anode candidates because of their low cost and high capacities,[2–4] often significantly exceeding their theoretical values in the first discharge and resulting in extra capacities.[5–10] In the last two decades,[11] despite tremendous effort in both mechanistic investigation and materials engineering with certain performance enhancements achieved, a generally accepted understanding of their lithiation phase behaviors has not yet been achieved.[12–17] In the absence of such mechanistic knowledge, diagnostic investigations of the extra capacities—even from the same material[5,8]—have alluded to fundamentally different causes, i.e., surface side reactions[5,7] versus space charge.[8,18] A systematic investigation of these oxides' initial discharge is therefore crucial to resolve these apparent contradictions.

Because $M_xO_y$ are considered conversion materials, i.e., which lithiate via reconstructive phase transitions, their lithiation usually exhibits heterogeneous and nanoscopic properties, giving rise to significant challenges in characterization for which

[1]Inorganic Chemistry Laboratory, University of Oxford, Oxford OX1 3QR, UK

[2]School of Chemistry, University of Birmingham, Birmingham B15 2TT, UK

[3]Departamento Química Inorgánica, Universidad Complutense de Madrid, 28040 Madrid, Spain

[4]Diamond Light Source Ltd., Harwell Science and Innovation Campus, Didcot OX11 0DE, UK

[5]Department of Materials, University of Oxford, Parks Road, Oxford OX1 3PH, UK

[6]Department of Chemistry, University of Oxford, Mansfield Road, Oxford OX1 3TA, UK

[7]Twitter: @xiaohua716

[8]Lead contact

*Correspondence: xiaohua716@gmail.com

https://doi.org/10.1016/j.xcrp.2021.100543

non-routine experimental methods are required. Recent instrumental advances have expanded the frontier of structure measurement to atomic precision using modern crystallographic techniques, e.g., pair distribution function (PDF) analysis.[19] Nevertheless, reliable and robust structure identification of a multi-phase system—particularly when some species either adopt non-equilibrium structures or are interrelated by phase transitions—remains a practical challenge. To circumvent this challenge, we combine PDF with Metropolis non-negative matrix factorization (NMF),[20] a novel analytical approach developed for mixed-phase deconvolution with no requirement of prior knowledge of the material system concerning the number and the nature of the phases.[21] We apply this methodology to a series of $Fe_xO_y$ (FeO, $Fe_3O_4$, and $\alpha$-$Fe_2O_3$) and $Mn_xO_y$ (MnO and $Mn_3O_4$) phases as model systems for a comparative study, because their reversible cycles (after the first discharge) show a metal-dependent behavior.[22] In addition, although the lithiation of $M_xO_y$ is dominated by two-phase reactions, some non-divalent $M_xO_y$ phases experience additional single-phase insertion processes upon initial discharge,[12,23–25] giving rise to a rich mechanistic variation ideal for testing the practicability, as well as establishing the protocol, of our method on complex systems.

Our analyses across the $Fe_xO_y$ series uncovered an unexpected and consistent formation of body-centered cubic (*bcc*) $FeO_x$ ($0 \leq x \leq 1$) solid solution, a phase that is challenging to access via conventional analytical procedures and that has been unanimously perceived as $\alpha$-Fe or rocksalt (*rs*)-type FeO in the literature;[8,16,17,24,26] we additionally observed a particle-grinding process in both $Mn_xO_y$ materials that shows no sign of Mn redox. This electrochemical pulverization and the *bcc*-$FeO_x$ phase transition take place at early and late discharge, respectively, in association with the observed extra capacities, likely implying their different origin between $Fe_xO_y$ and $Mn_xO_y$. In light of this metal-dependent nature, together with the $FeO_x$ solid-solution behavior that underpins the reversibility of $Fe_xO_y$,[22] we challenge the space charge (or interfacial storage) model[6,18]—whereby the extra capacity of metal oxides arises from surface capacitance of metal nanoparticles—which was reinforced by a magnetometry study.[8] Although our study suggests strong correlation between the electrolyte/surface side reactions[7,9] and these additional capacities, there are several viable mechanisms at play, with the dominant factor determined by the specific metal species involved. Therefore, our renewed discharge phase behaviors of $M_xO_y$ serve as an important crystallographic and mechanistic reference from which to revisit previous studies and elucidate fully the extra capacity at low voltage. From a methodological perspective, this work demonstrates the robustness, flexibility, and reliability of the NMF approach to explore mechanistically highly convoluted chemical and electrochemical reactions, with a broad implication not only in a range of battery chemistries (e.g., alloy, displacement, and insertion) but also in fields beyond energy storage (e.g., catalysis and materials engineering).

## RESULTS

### Selection of metal oxides

Among the selected metal oxides, $\alpha$-$Fe_2O_3$ experiences the most complex lithiation, because it additionally involves oxide rearrangement from hexagonal close-packed (*hcp*) to face-centered cubic (*fcc*) configuration.[24] We therefore chose to elaborate the investigation of $\alpha$-$Fe_2O_3$ step by step to demonstrate the analytical protocol, using which the other oxides were then studied systematically. Because of the expected mechanistic difference between MO and $M_3O_4$ phases (M = Fe and Mn), our studies of these two series are described separately. Unless stated otherwise,
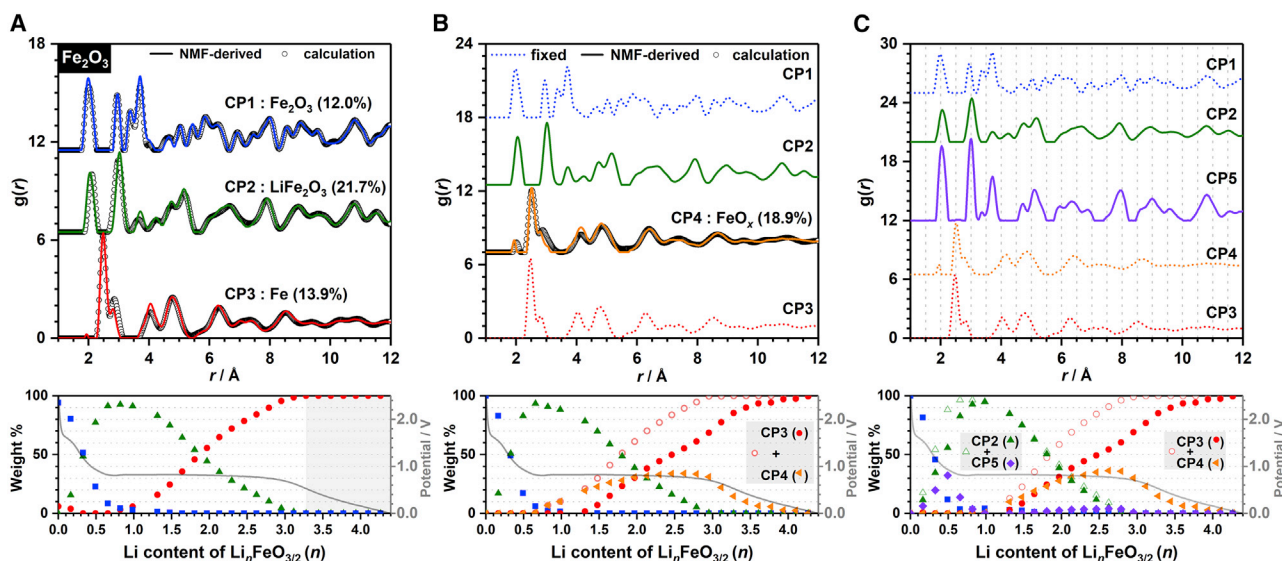
**Figure 1. NMF analysis of discharged α-Fe$_2$O$_3$ employing different numbers of components**

(A) Analysis using three CPs (see also Video S1).

(B) Analysis using four CPs (see also Video S2).

(C) Analysis using five CPs (see also Video S3).

The corresponding ratios from each analysis are shown at the bottom (colored hollow circles and triangles in B and C correspond to the summation of the ratios using the specified CPs). For easy comparison between different metal oxide species, the x axes of the galvanostatic profiles in this work are all plotted against normalized Li content, meaning the number of Li is weighted against the number of metal centers (x) in M$_x$O$_y$ (M = Fe and Mn), i.e., the full (theoretical) capacity for α-Fe$_2$O$_3$ corresponds to 3 Li per FeO$_{3/2}$. The shaded area in (A) denotes the extra capacity. The CPs randomly parameterized and derived from the analysis are denoted by solid lines, whereas the CPs constrained during the analysis are denoted by dotted lines. The labeled phases are tested via refinement and compared with the calculated patterns denoted by black circles. The color code to represent distinct phases (or CPs) is consistent.

all analyses were performed on the *in operando* PDF data series acquired during these materials' first discharge.

## α-Fe$_2$O$_3$

Our initial NMF analysis was based on an assumption of no prior knowledge of the system. Consequently, three randomly defined components (hereafter shortened to CP) were employed, corresponding to the two end phases of the lithiation reaction and a single additional intermediate phase—the only constraint applied in this analysis was the number of phases (i.e., three). Following this, we add one CP (representing a new intermediate structure) in every subsequent analytical step. The initial three-CP analysis (Video S1) returned distinct patterns (Figure 1A) for the starting, intermediate, and end phases, which can be modeled by α-Fe$_2$O$_3$ (R-3c), LiFe$_2$O$_3$ (Fm-3m), and α-Fe (Im-3m, 2 nm particles), respectively. The evolution of their phase ratios echoes the reported two-step lithiation from α-Fe$_2$O$_3$ to Fe nanoparticles via a rs-related Li$_y$Fe$_x$O$_2$ intermediate (however, its composition and structure vary among different studies).[23,24,26] In addition, the PDF data reconstructed based on the NMF output exhibit excellent agreement with the experimental patterns (Figure S1).

To explore the presence of any additional phase (or structure modification), a four-CP analysis was performed, with the potential extra phase assigned to the 4th CP. Because the two end members of the lithiation (α-Fe$_2$O$_3$ and Fe) have been firmly established, their respective CPs were defined using the experimental data (i.e., the first and the last pattern of the experimental PDF series) and were constrained
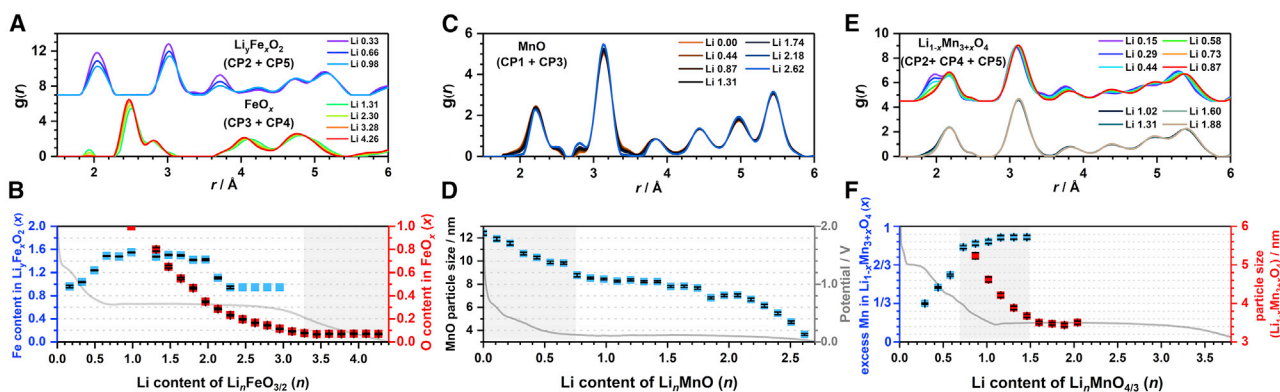
**Figure 2. Understanding the NMF-derived components**

(A) PDF reconstruction of $Li_yFe_xO_2$ and $bcc$-$FeO_x$ intermediate phases using the specified CPs derived from Figure 1C.

(B) Evolution of the Fe content ($x$) in $Li_yFe_xO_2$ (blue) and the oxygen content ($x$) of $bcc$-$FeO_x$ (red) derived from refinement.

(C) PDF reconstruction of MnO using the NMF output from Figure 3C.

(D) Evolution of the MnO particle size derived from refinement.

(E) PDF reconstruction of $Li_{1-x}Mn_{3+x}O_4$ using the NMF output from Figure 4D.

(F) Evolution of excess Mn ($x$) in $Li_{1-x}Mn_{3+x}O_4$ (blue) and its particle size (red) derived from refinement.

The shaded area denotes extra capacity. The standard deviations of the refined parameters are denoted by error bars.

during the analysis (denoted by dotted lines in Figure 1B and thereafter). The other two CPs, considered unknown, were randomly assigned and were subsequently resolved by NMF analysis (Video S2). The results (Figure 1B) unsurprisingly show one pattern that agrees with the $LiFe_2O_3$ phase (CP2); the other component (CP4) appears analogous to Fe (CP3) except for (1) a discernible increase in peak positions to higher r and (2) a new atom pair emerging at a separation of around 1.9 Å. These two features—attributed to (1) an expanded Fe sublattice resulting from accommodation of $O^{2-}$ and (2) an average O-Fe distance of the distorted $OFe_6$ octahedra, respectively—distinguish themselves from structural characteristics of either $\alpha$-Fe ($bcc$) or $rs$-type FeO, pointing to a rare iron monoxide polymorph $bcc$-FeO, which we recently identified upon charging of $Fe_xO_y$.[22] The total ratio of $bcc$-FeO and Fe (denoted by a red circle in Figure 1B) is consistent with the Fe weighting derived from the initial three-CP analysis. On the one hand, this observation demonstrates the high sensitivity of the NMF algorithm that allows decoupling of phases with subtle structural differences; on the other hand, it suggests an underlying correlation between $bcc$-FeO and Fe that is likely underpinned by a solid-solution reaction via $bcc$-$FeO_x$ ($1 \geq x \geq 0$).[22] The systematic change of interatomic distances and thus a continuous shift of PDF peaks could be qualitatively represented by mixing of the two end members.

Based on the four-CP results, we proceeded with a five-CP analysis by including a new unknown CP. The as-identified $bcc$-FeO intermediate was constrained, together with the two end-member phases (Video S3). For the two remaining unknown CPs, the analysis returned two similar patterns, with one (CP2) agreeing with $LiFe_2O_3$ and the other (CP5) differing only in peak intensities (Figure 1C). According to their phase ratios, these two CPs, likely jointly representing $Li_yFe_xO_2$, are correlated in a similar manner to that between $bcc$-FeO and Fe. These correlations manifest themselves more evidently in the reconstructed PDFs (Figure 2A) as continuous peak changes. We tested this theory via refinement, confirming that the $Li_yFe_xO_2$ and $bcc$-$FeO_x$ series could be modeled by using cation-disordered $\alpha$-$Li_{2-x}Fe_xO_2$ ($Fm$-$3m$) and tetragonally distorted $FeO_x$ rocksalt ($I4/mmm$)[27] solid solutions, respectively, and that the systematic variations in peak intensities and
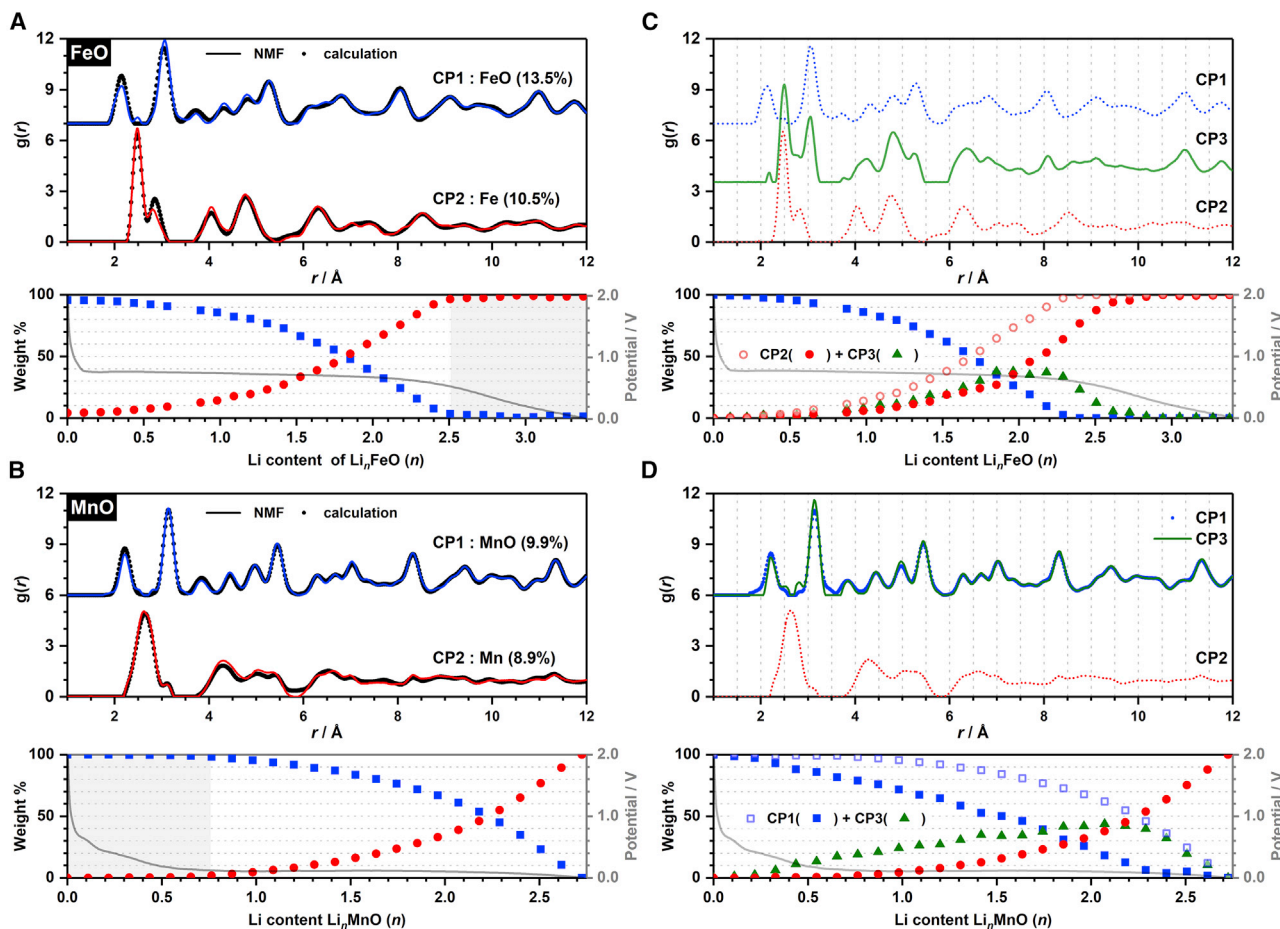
**Figure 3. NMF analysis of discharged FeO and MnO**
(A and C) Two- and three-CP NMF analysis of discharged FeO.
(B and D) Two- and three-CP NMF analysis of discharged MnO.
The corresponding ratios are shown at the bottom. The styling follows the same format as Figure 1.

positions (Figure 2A) could be rationalized by coherent changes in phase compositions (Figure 2B) and lattices (Figure S2A) during the Li insertion and solid-solution evolution, respectively. We note the surprising presence of $bcc$-FeO$_x$ during discharge, given that earlier studies unanimously reported a direct extrusion of $\alpha$-Fe from the intermediate Li$_y$Fe$_x$O$_2$.[23,26,28] However, not only could the employment of this $bcc$-FeO phase significantly improve the refinement (Figure S2B), but its distorted Fe sublattice (due to hosting O$^{2-}$) and the two-step solid-solution behavior[22] also could account for the reported defective Fe structure[26] and successive formation of two types of Fe nanoparticles upon lithiation,[15] respectively, reconciling the inconsistency highlighted previously in the literature.

**FeO and MnO**
Turning to the divalent metal monoxides, our initial analysis included only two unconstrained CPs based on an assumption of no intermediates. The NMF-derived CPs exhibit distinct patterns corresponding to $rs$-type FeO/MnO and $\alpha$-Fe/$\alpha$-Mn phases whose evolutions reveal an inactive regime in both materials (shaded area in Figures 3A and 3B). This regime is associated with considerable capacity ($\geq 0.8$ Li per metal center) that shows no apparent connection with these oxides' phase evolution, contributing to the additional (or extra) capacity that has been extensively
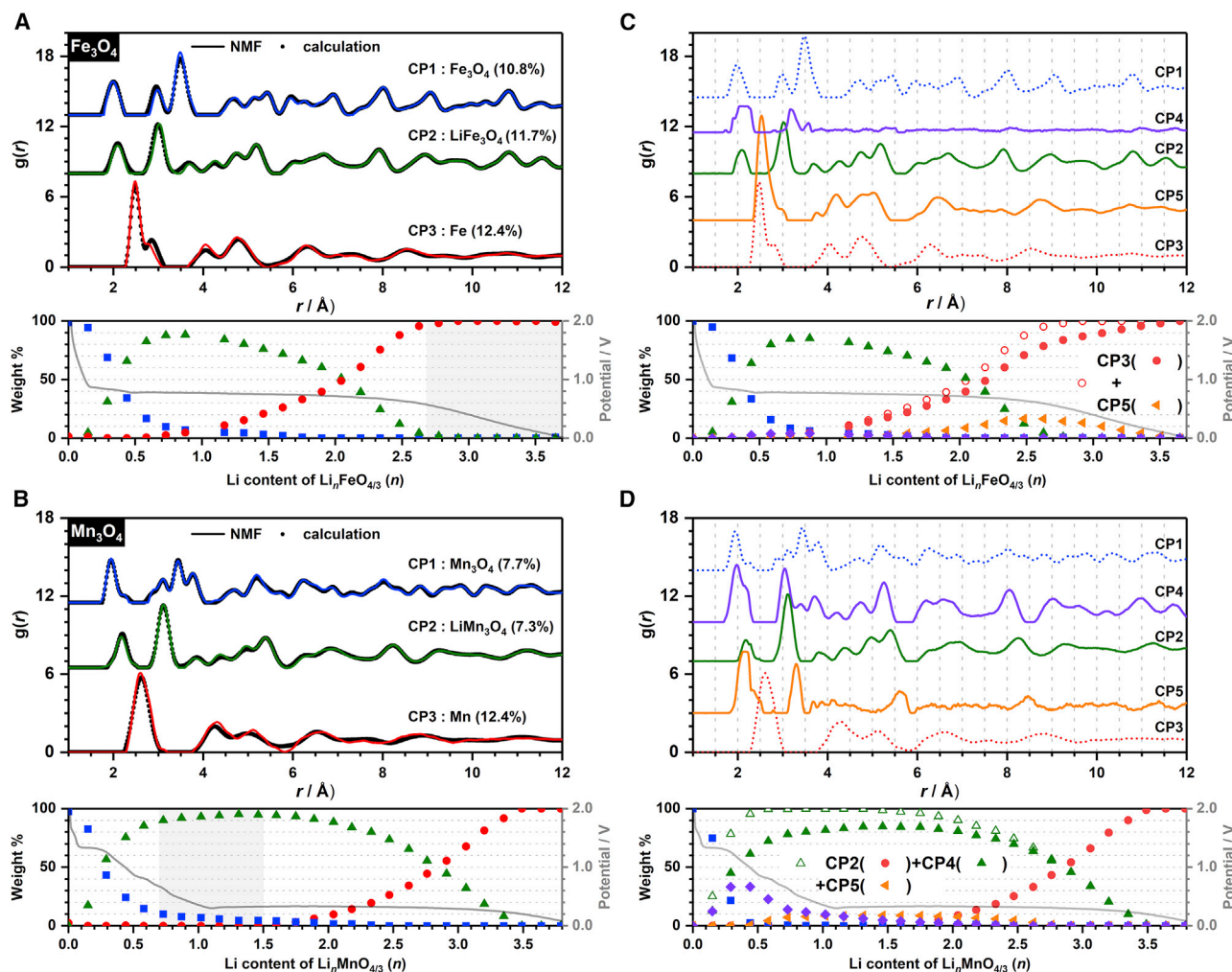
**Figure 4. NMF analysis of discharged $Fe_3O_4$ and $Mn_3O_4$**
(A and C) Three- and five-CP NMF analysis of discharged $Fe_3O_4$.
(B and D) Three- and five-CP NMF analysis of discharged $Mn_3O_4$.
The corresponding ratios are shown at the bottom. The styling follows the same format as Figure 1.

studied in the battery community.[7,8,16,18,29] Although this additional capacity is commonly observed at the end of discharge,[7,8] i.e., in FeO and $\alpha$-$Fe_2O_3$, it occurs unexpectedly at the beginning of lithiation for MnO, indicating the nature and the origin of this extra capacity are different for the two metals. We return to this point in the Discussion.

To examine a possible intermediate phase, three-CP analysis was performed with the as-identified MO and M phases constrained. Judging by the derived ratios (Figures 3C and 3D), the newly deconvoluted CP3 in the FeO and MnO systems appears to be correlated with Fe (CP2) and MnO (CP1), respectively. This CP3 pattern in FeO is complexed with rocksalt features (i.e., peaks at 3.1 and 5.3 Å), with the rest of the peaks consistent with the $bcc$-FeO uncovered in $\alpha$-$Fe_2O_3$. Verified by refinements (Figure S3A), we confirm the presence of the $bcc$-$FeO_x$ series with the highest (nominal) Fe oxidation state likely lower than +2 ($x < 1$) given its formation upon the reduction of FeO. In MnO, by contrast, the CP3 pattern looks almost identical to that of the parent MnO, with a marginal variation in peak intensities that could be more readily
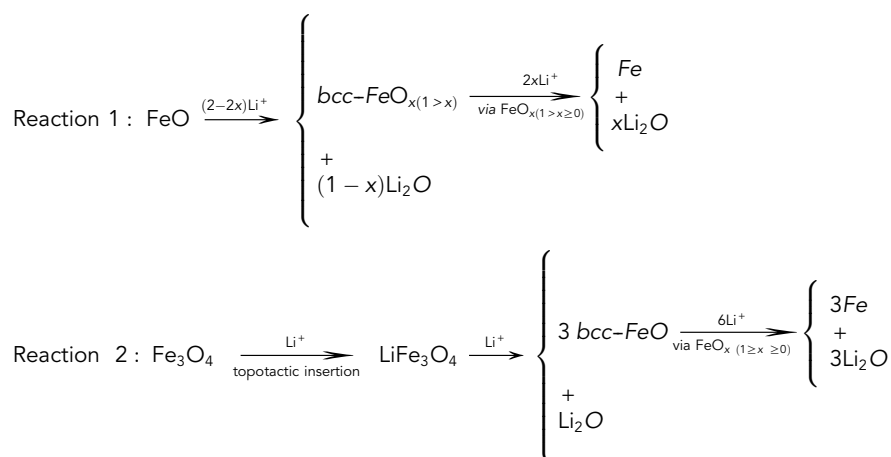
seen in the reconstructed PDFs (Figure 2C). As confirmed by refinement (Figure 2D), these intensity variations are an indication of particle size reduction,[30] which occurs throughout the first discharge. Although size reduction would be expected for conversion materials in the first discharge because of their reconstructive phase transitions,[2] its occurrence in association with the extra capacity underlines their potential correlation.
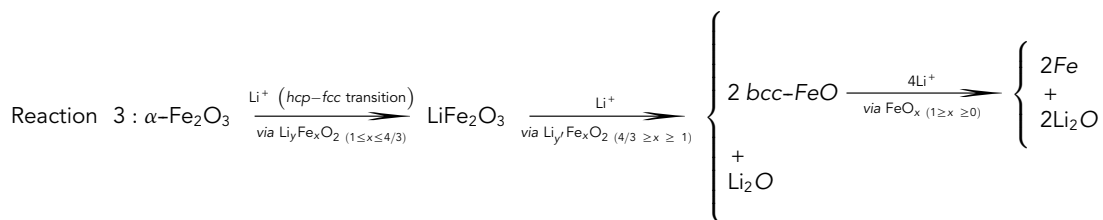
### $Fe_3O_4$ and $Mn_3O_4$

Our initial analysis of $Fe_3O_4$ and $Mn_3O_4$ assumed one intermediate phase for each system and hence included three unconstrained CPs. Their resulting patterns could be well modeled by $Fe_3O_4/Mn_3O_4$ (CP1), $\alpha$-Fe/$\alpha$-Mn (CP3), and $LiFe_3O_4$ (*Cmmm*)/ $LiMn_3O_4$ (*C2/m*) as the intermediate phases (CP2 in Figures 4A and 4B). In light of the results of $\alpha$-$Fe_2O_3$ requiring five CPs to fully describe its phase behavior, we directly proceeded with a five-CP analysis, during which only the two end-member phases ($M_3O_4$ and M) were constrained. For $Fe_3O_4$ (Figure 4C), two among the three resulting patterns agree with $LiFe_3O_4$ (CP2) and *bcc*-FeO (CP5) as expected, whereas CP4 is associated with a negligible ratio whose pattern also lacks distinct physical meaning. These observations, supported by refinement, confirm the presence of *bcc*-$FeO_x$ (Figure S3B) and the adequacy of four CPs to describe $Fe_3O_4$'s lithiation. Our identification of the $LiFe_3O_4$ phase is consistent with a recent transmission electron microscopy (TEM) study,[31] despite all earlier reports[23,25,32] having suggested a $Li_xFe_3O_4$ phase with a maximum Li content (x) of 2.

For $Mn_3O_4$ (Figure 4D), the three deconvoluted CPs all show patterns comparable to $LiMn_3O_4$ (CP2), with negative and positive peak shifts observed for CP4 and CP5, respectively. An evaluation of their reconstructed PDFs (Figure 2E) followed by verification via refinement (Figure 2F) showed that the overall variations of these patterns follow two steps. The first pathway corresponds to a $Li_{1-x}Mn_{3+x}O_4$ solid-solution process until reaching a composition of MnO (x ≈ 1); this electrochemically formed MnO subsequently undergoes pulverization with no discernible sign of phase transformation, contributing to additional capacity (≈0.8 Li per metal center) in the same way as the pristine MnO, confirming the link between the pulverization of MnO and the extra capacity.

### DISCUSSION

Reaction 1 : $FeO \xrightarrow{(2-2x)Li^+}$ 
$$\begin{cases} bcc\text{-}FeO_{x(1>x)} \xrightarrow[\text{via } FeO_{x(1>x\geq0)}]{2xLi^+} \begin{cases} Fe \\ + \\ xLi_2O \end{cases} \\ + \\ (1-x)Li_2O \end{cases}$$

Reaction 2 : $Fe_3O_4 \xrightarrow[\text{topotactic insertion}]{Li^+} LiFe_3O_4 \xrightarrow{Li^+}$ 
$$\begin{cases} 3\ bcc\text{-}FeO \xrightarrow[\text{via } FeO_x\ (1\geq x\ \geq0)]{6Li^+} \begin{cases} 3Fe \\ + \\ 3Li_2O \end{cases} \\ + \\ Li_2O \end{cases}$$

$$\text{Reaction} \quad 3 : \alpha\text{-Fe}_2\text{O}_3 \xrightarrow[\text{via Li}_y\text{Fe}_x\text{O}_2 \, (1 \leq x \leq 4/3)]{\text{Li}^+ \, (hcp - fcc \, \text{transition})} \text{LiFe}_2\text{O}_3 \xrightarrow[\text{via Li}_{y'}\text{Fe}_x\text{O}_2 \, (4/3 \, \geq x \, \geq \, 1)]{\text{Li}^+} \begin{cases} 2 \, bcc\text{-}FeO \xrightarrow[\text{via FeO}_x \, (1 \geq x \, \geq 0)]{4\text{Li}^+} \begin{cases} 2Fe \\ + \\ 2\text{Li}_2O \end{cases} \\ + \\ \text{Li}_2O \end{cases}$$

The key mechanistic difference among $\text{FeO}$, $\text{Fe}_3\text{O}_4$, and $\alpha$-$\text{Fe}_2\text{O}_3$ lies in the presence and the nature of the initial insertion process. Although this process is absent from $\text{FeO}$ (reaction 1), the insertion mechanism significantly varies between $\text{Fe}_3\text{O}_4$ and $\alpha$-$\text{Fe}_2\text{O}_3$. In $\text{Fe}_3\text{O}_4$ (reaction 2), it undergoes a two-phase reaction forming $\text{LiFe}_3\text{O}_4$ via topotactic $\text{Li}^+$ insertion; subsequent lithiation of $\text{LiFe}_3\text{O}_4$ results in the extrusion of $bcc$-$\text{FeO}$ (and $\text{Li}_2\text{O}$). In contrast, the insertion process in $\alpha$-$\text{Fe}_2\text{O}_3$ (reaction 3, Figure 5A) appears significantly more intricate, because it involves (1) transformation of oxide sublattice from $hcp$ in $\alpha$-$\text{Fe}_2\text{O}_3$ to $fcc$ in $\text{Li}_y\text{Fe}_x\text{O}_2$ and (2) a concurrent solid-solution process via the $\text{Li}_y\text{Fe}_x\text{O}_2$ ($y = 2 - x$) intermediate whose Fe content ($x$) increases from ca. 1 to 4/3, corresponding to nominal compositions of $\text{LiFeO}_2$ and $\text{LiFe}_2\text{O}_3$, respectively. Further lithiation of $\text{LiFe}_2\text{O}_3$ triggers the extrusion of $bcc$-$\text{FeO}$ (and $\text{Li}_2\text{O}$), whereas the parent phase retains the solid-solution behavior via $\text{Li}_y\text{Fe}_x\text{O}_2$ ($y' = 2 - x$), where the change of Fe content (Figure 2B) mirrors that in the $\text{Li}_y\text{Fe}_x\text{O}_2$ series (as denoted by $y'$ in the formula and illustrated using a different color gradient in Figures 5A and 5C). The coexistence of the two solid-solution series is likely driven by a phase separation of the $\text{Fe}^{3+}$ and $\text{Fe}^{2+}$ species that dominate the $\text{Li}_y\text{Fe}_x\text{O}_2$ and $\text{FeO}_x$ phases, respectively.

Subsequent lithiation of $bcc$-$\text{FeO}_x$ follows the same pathway in $\text{FeO}$, $\text{Fe}_3\text{O}_4$, and $\alpha$-$\text{Fe}_2\text{O}_3$ via topotactic extraction of $\text{O}^{2-}$ from the Fe sublattice (to form $\text{Li}_2\text{O}$ on the $\text{FeO}_x$ surface; Figure 5C, process I).[22] According to the refinement (Figures S2A and S4), this $\text{FeO}_x \rightarrow \text{Fe}$ phase transition likely occurs via two steps, following an order-to-disorder transition (with respect to the $\text{O}^{2-}$ distribution within the Fe sublattice; Figure 5C, process II) that governs the lithiation reaction in the reversible cycles of $\text{Fe}_x\text{O}_y$.[22] Note that given the distorted nature of the $\text{FeO}_x$ nanoparticle (ca. 2 nm), complexed with the oxygen contribution from $\text{Li}_2\text{O}$ (ca. 3 nm), precise determination of the oxygen content ($x$) is difficult. Thus, the preceding reactions involving $\text{FeO}_x$ correspond to an idealized and simplified representation.

$$\text{Reaction} \quad 4 : \text{MnO} \xrightarrow[\text{pulverisation}]{(\text{Li}^+)} \text{MnO}_{nano} \xrightarrow{2\text{Li}^+} \begin{cases} Mn \\ + \\ \text{Li}_2O \end{cases}$$

$$\text{Reaction} \quad 5 : \text{Mn}_3\text{O}_4 \xrightarrow[\text{topotactic insertion}]{\text{Li}^+} \text{LiMn}_3\text{O}_4 \xrightarrow[\text{via Li}_{1-x}\text{Mn}_{3+x}\text{O}_4 \, (0 \, \leq \, x \, \leq 1)]{\text{Li}^+} \begin{cases} 3MnO \xrightarrow[\text{pulverisation}]{(\text{Li}^+)} 3MnO_{nano} \xrightarrow{6\text{Li}^+} \begin{cases} 3Mn \\ + \\ 3\text{Li}_2O \end{cases} \\ + \\ \text{Li}_2O \end{cases}$$
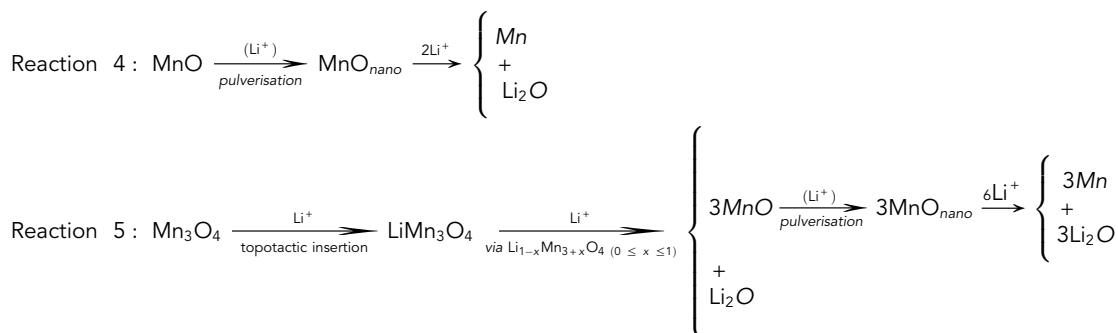
For the Mn series, the initial insertion is only seen in $\text{Mn}_3\text{O}_4$ (reaction 5), which occurs topochemically, forming $\text{LiMn}_3\text{O}_4$ via a two-phase pathway. Further Li incorporation triggers phase separation between $\text{Li}_2\text{O}$ and the Mn-rich domain, the latter

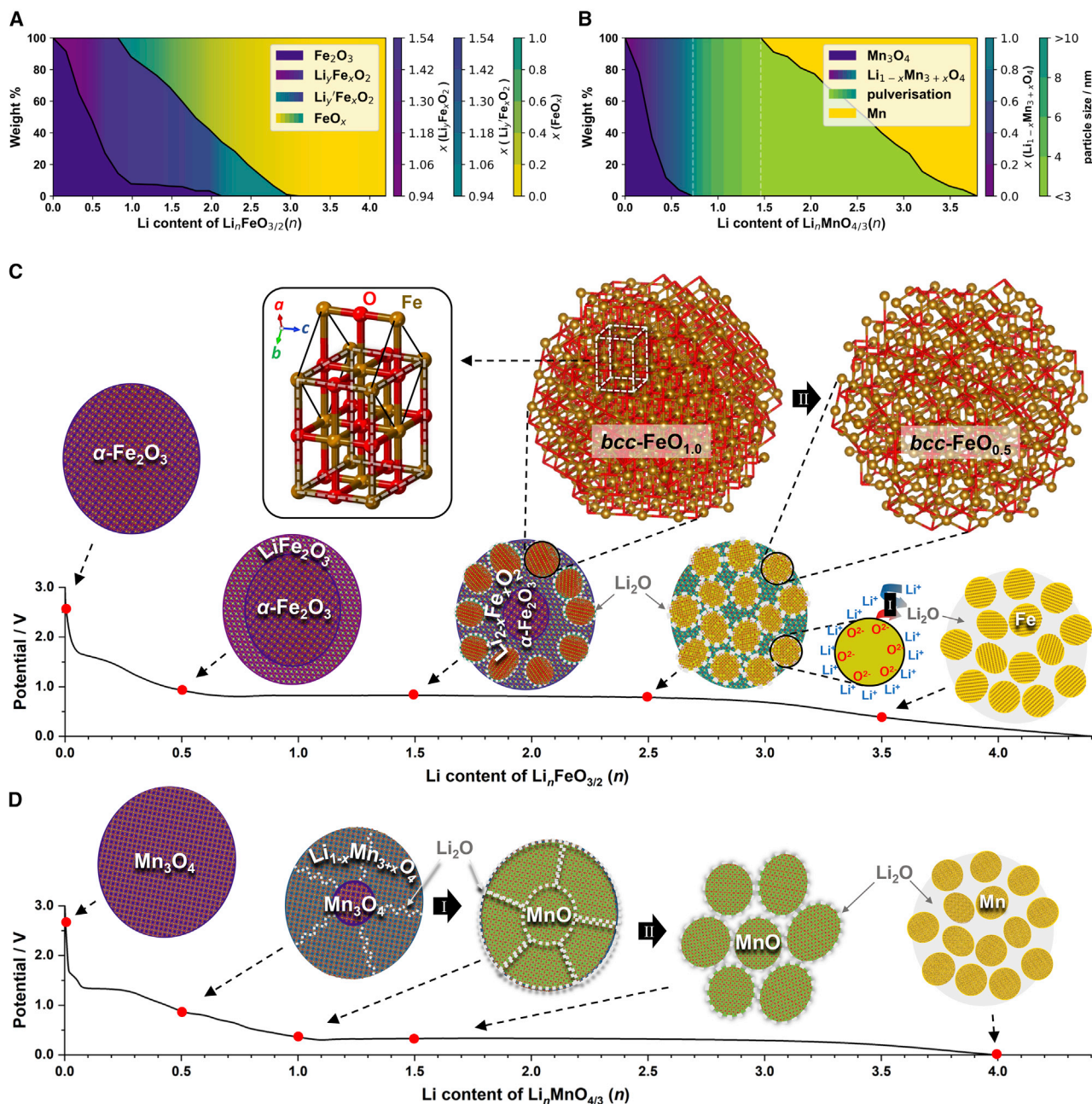**Figure 5. Lithiation phase behaviors of $\alpha$-Fe$_2$O$_3$ and Mn$_3$O$_4$**

(A and B) Phase behaviors based on the phases identified via NMF and quantified via refinement.

(C and D) Corresponding schematic illustrations at selected states of discharge (indicated by black dashed arrows and red circles). Background colors of the phases reflect their compositions at the same states of discharge shown in (A) and (B).

In (A), color gradients purple → indigo and cyan → indigo, respectively, denote increased Fe composition ($x$) in Li$_y$Fe$_x$O$_2$ and Li$_{y'}$Fe$_x$O$_2$ solid-solution series, whereas cyan → yellow corresponds to $bcc$-FeO$_x$ with reduced oxygen content. In (B) and (D), gradient purple → cyan/process I and gradient cyan → green/process II, respectively, denote increased excess Mn ($x$) in Li$_{1-x}$Mn$_{3+x}$O$_4$ and its reduced particle size ($x = 1$), with the white dashed lines highlighting this pulverization process in (B). Li$_2$O phases are simplified by using gray dashed lines and circles. In (C), the equivalent representation of the surface charge model is indicated by process I, whereas process II suggests an order-to-disorder transition with respect to the oxygen distribution in the $bcc$-FeO$_{1.0}$ and $bcc$-FeO$_{0.5}$ phases obtained by Monte Carlo simulation[22] (without considering the surface structures). Red and yellow balls/sticks denote oxygen and iron atoms/bonds, respectively. White dashed lines highlight a tetragonally distorted $rs$-FeO unit cell, in which the $bcc$-Fe unit is also highlighted using black lines.

undergoing a simultaneous transformation via $Li_{1-x}Mn_{3+x}O_4$ ($0 \leq x \leq 1$) solid solution (Figure 5B), where Mn progressively substitutes Li (in the $2c$ site of the $C2/m$ structure) until reaching a composition $x \approx 1$ to form the $rs$-type MnO. Despite comparable onset of insertion between $Fe_3O_4$ and $Mn_3O_4$, a prominent solid-solution intermediate is only observed in $Mn_3O_4$. Its monophasic phase transition allows the derived $rs$-MnO to largely retain the parent structure's coherent length (Figure 5D, process I), in striking contrast with the extruded $bcc$-FeO, which has very small sizes. Although the particle size of this $rs$-MnO decreases upon further reaction (Figure 5D, process II), we highlight that this size reduction is not a result of lithiation (of the particle), as previously reported,[12] but rather an unexpected outcome of a secondary process that also occurs in pristine MnO (reaction 4). The fully converted metal nanoparticles (ca. 2 nm) and $Li_2O$ (ca. 3 nm) show sizes comparable to those in $Fe_xO_y$.

All three non-divalent metal oxides transform into a rocksalt-type $Li_{1-x}M_xO_2$ (M = Fe and Mn) intermediate upon initial Li reaction. Although these intermediates in $Fe_3O_4$ and $Mn_3O_4$ have a relatively ordered cation distribution, the $hcp \rightarrow fcc$ transition in the O sublattice of $\alpha$-$Fe_2O_3$ leads to a cation-disordered rocksalt (DRX) $LiFe_2O_3$, which is electrochemically active within the voltage window of 4.0–1.5 V.[24] Although some DRX materials can be obtained thermally at reasonable temperatures, for some compositions, to introduce disorder requires extensive mechanical forces via ball-milling.[33] Given the important discoveries of the DRX materials in cathode and anode applications,[34–36] the unique phase behavior observed in $\alpha$-$Fe_2O_3$ suggests a viable new route to electrochemically access the cation disorder.[35]

A recent study on the solid-electrolyte-interphase (SEI) chemistry of metal oxide anode (based on NiO as the model compound) confirmed that the electrolyte side reactions take place alongside oxide's conversion throughout its reaction voltage window (1–0 V) and can be divided into several mechanistically distinct stages at different depths of lithiation, including the beginning and the end of discharge.[9] This suggests a correlation, at least partly, between these electrolyte reactions and the extra capacities observed in $Fe_xO_y$ (ca. 1.0–1.3 Li per Fe) and $Mn_xO_y$ (ca. 0.8 Li per Mn), because they are observed below 1 V. For the Mn oxides in particular, because of the concomitant particle grinding of the MnO phase, we infer that this MnO (or $Mn^{2+}$) plays a catalytic role in exacerbating the extra capacity, given the reduced particle size; hence, the larger surface area may prompt more electrolyte side reactions. Although the nature of these reactions cannot be confirmed, it should be fundamentally different from the space charge (or interfacial storage) mechanism,[6,29] a theory reinforced by a magnetometry study (of $Fe_3O_4$)[8] in which a systematic change of magnetic moment of the metal oxide electrode was detected upon cycling and was attributed to a surface storage of $e^-$ on the converted metal nanoparticles (and hence a capacitive response). Although we may not rule out the possibility of a surface capacitance on the Mn nanoparticles at the end of discharge (i.e., <0.2 V), we can confirm that these surface $e^-$, if they exist, do not constitute the main source of the extra capacity in the Mn oxides.

We also point out that the space charge theory requires "no phase changes or formation of iron oxide"[8] upon charging of $Fe_xO_y$. Although this criterion seems to be fulfilled based on the lack of (long-range) structural change in the reported X-ray diffraction (XRD) results,[8] our own PDF analysis suggests the Fe $\rightarrow$ $bcc$-FeO redox reaction occurs.[22] Together with the unexpected observation of this $bcc$-FeO during the first discharge, our renewed mechanistic understanding of $Fe_xO_y$ challenges that phase-behavior criterion and offers an alternative rationale to the reported results in that magnetometry study.[8] By way of example, given the solid-solution behavior of

$bcc$-FeO$_x$—a phase that deviates from the thermodynamically stable structure—one cannot simply exclude the possibility of non-equilibrium species, such as Fe$^+$ (3$d^7$) and/or O$^-$ (2$s^2$2$p^5$), formed during the phase transition. Both species have an unpaired electron or electrons that could justify the detected magnetic moment. In addition, the accumulation of O$^{2-}$ (or O$^-$) at the FeO$_x$/Li$_2$O interface for the Li$^+$ reaction provides an equally sensible surface charge model (Figure 5C, process I) to account for the observed capacitive behavior.

Based on our prior study[22] of the same series of materials on their charging process, as well as subsequent cycles, their reversible capacities are dominated by reactions between Fe/Mn and $bcc$-FeO/$zincblende$-MnO, suggesting the extra capacity observed during the initial discharge is largely irreversible. Even if excess storage of $e^-$ does occur on the particle surface and contribute to a reversible extra capacity, it does not necessarily preclude the capacity contribution from the electrolyte[9] and/or the LiOH surface reactions[7] observed in the NiO and RuO$_2$ systems, respectively. Given the metal-dependent nature demonstrated in this study, this extra capacity is likely a result of several causes, with the dominant source depending on the specific metal species. In light of our renewed discharge mechanism of Fe$_x$O$_y$ and Mn$_x$O$_y$, as well as our recently discovered reversible formation of non-equilibrium FeO and MnO phases that underpin these materials' reversibility in subsequent cycles,[22] it is important to revisit earlier diagnostic studies and develop further a comprehensive understanding of the low-voltage discharge capacities.

As a multivariate method, Metropolis NMF delivers solutions to experimental datasets (of size $m$) in the form of linear combinations of $n$ fundamental components ($m > n$).[21] This principle renders our methodology ideal for the study of two-phase reactions in which each phase's structure is independent of its mixing ratio. However, we also demonstrate the viability of this method to explore solid-solution processes in which a continuous and monophasic phase change occurs across lithiation or delithiation. Because of the non-negative constraints employed in the algorithm, the PDF patterns of the NMF-derived components are physically meaningful and directly point to actual phases or structure modifications, paving the way for a robust phase analysis. This methodological advantage appears more evident when our approach is compared with the state-of-the-art technique, namely, principal-component analysis (PCA).[37–40]

To demonstrate our point, we reanalyzed our $\alpha$-Fe$_2$O$_3$ data using the PCA approach.[37] As its algorithm forces its components (denoted as CP$_{PCA}$) to be mutually orthogonal, the derived CP$_{PCA}$ and the weightings often show negative values (Figures 6A and 6B) and therefore are not physically meaningful. Although ideally meaningful patterns could still be produced via reconstruction (Figure 6C), to do this requires the number of CP$_{PCA}$ predetermined based on their eigenvalues (Figure 6A). These values are an unbiased estimate of the significance for each CP$_{PCA}$; however, their evaluation, and hence the determination of the number of CP$_{PCA}$, is rather intuitive, rendering the PCA method susceptible to exclusion of minor, albeit important, components. For example, we show that the PCA results for the $\alpha$-Fe$_2$O$_3$ system suggest three, but not five, CPs (CP1–CP3 in Figure 6A). Although they seem sufficient to describe the three key phases, information concerning the two solid-solution series (likely concealed in CP4 and CP5) is lost—including the structural fingerprints that support $bcc$-FeO$_x$. Furthermore, the reconstruction requires the CP$_{PCA}$ coefficients for each phase to be individually decoupled from the overall weighting. This is challenging for systems with multiple coexisting phases when their CP$_{PCA}$ coefficients are both unknown and correlated. Thus, in practice, to
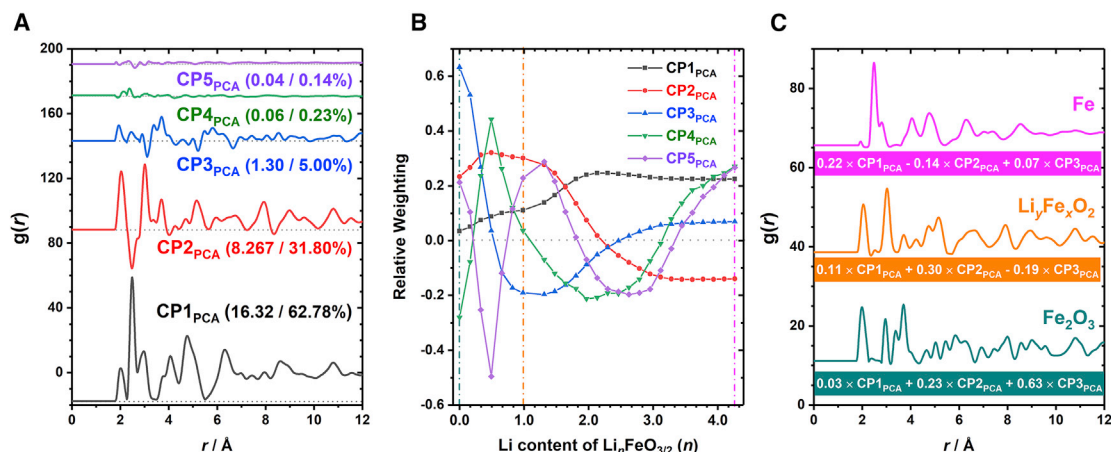
**Figure 6. PCA of discharged α-Fe$_2$O$_3$**

(A and B) The five most significant components (CP$_{PCA}$) obtained from the PCA of the α-Fe$_2$O$_3$ data series and their weightings. Black dotted lines mark the zero line for each CP$_{PCA}$ to show their negative values. The values in the brackets correspond to eigenvalues ($\lambda_i$) and the percentage of variance

($s_i = \lambda_i / \sum_{i=1}^{n} \lambda_i$) of each CP$_{PCA}$, according to which CP4$_{PCA}$ and CP5$_{PCA}$ are both unimportant.

(C) PDFs of the three phases reconstructed using CP1$_{PCA}$, CP2$_{PCA}$, and CP3$_{PCA}$. Their coefficients are determined based on an assumption of 100% of α-Fe$_2$O$_3$ (green), Li$_y$Fe$_x$O$_2$ (orange), and Fe (pink) at the beginning, Li 1.0, and the end of discharge, respectively (marked by dash-dotted lines in B).

reconstruct key phases (Figure 6B) would require an assumption of their 100% concentration at a rather biased selection of data points (Figure 6C). For instance, the reconstructed Li$_y$Fe$_x$O$_2$ was based on the postulate that the Li 1.0 sample was entirely composed of this intermediate—which deviates from the NMF and refinement results (Figures 1 and S5).

This comparative study reflects a less biased procedure using the NMF method and its better capability to disentangle highly correlated data, rendering NMF a more suitable and reliable approach for complex systems than the PCA method. Indeed, the NMF-derived phases could serve as reliable references for further quantitative handling of the data, but we highlight that even a preliminary analysis in the absence of prior knowledge of the material system can deliver key phases whose behaviors are accurate and comparable to the results from an in-depth refinement (Figure S5). This method is also resilient to the quality of the dataset, because it does not require data coherence from *in situ*/*in operando* experiments and is applicable to *ex situ* data series.[41] In addition, our approach uses the additivity nature of the PDF data, precluding the viability of the diffraction method (in the presence of correlated phase transitions). Although the analysis lays emphasis on atomic structures, this method would be equally effective for (highly) crystalline materials and feasible for other experimental techniques whose data also have additivity properties, e.g., spectroscopy.[42–44]

To summarize, we performed a systematic analysis of a series of discharged Fe$_x$O$_y$ and Mn$_x$O$_y$ using the Metropolis NMF approach to investigate their mixed-phase lithiation mechanism during the first discharge. In comparison to the conventional PCA method, we highlight the advantage of the NMF method in resolving highly correlated phases during their intricate phase transitions, involving both mono- and biphasic reactions and complexed with particle size reductions. This analytical advantage has led to our discovery of *bcc*-FeO$_x$ solid-solution and MnO pulverization processes, which are associated with the extra capacities observed at the late discharge of Fe$_x$O$_y$ and early lithiation of Mn$_x$O$_y$, respectively. In light of this

metal-dependent property, as well as the $bcc$-FeO$_x$ ($1 \geq x \geq 0$) single-phase behavior, we questioned the space charge model[8] used to rationalize the additional capacity and suggested the necessity of revisiting earlier studies based on our renewed phase behaviors of metal oxides. Although these model systems constitute a small (albeit important) family of energy storage materials, the potential of our method suggests its far-reaching implication for a range of battery chemistries and offers promising prospects for diverse applications beyond energy storage.

## EXPERIMENTAL PROCEDURES

### Resource availability

*Lead contact*

Further information and requests should be directed to and will be fulfilled by the lead contact, Xiao Hua (xiaohua716@gmail.com).

*Materials availability*

This study did not generate new unique materials.

*Data and code availability*

The published article includes all data analyzed and necessary to reach the conclusions of this study in the figures and tables of the main text and Supplemental information. Further information and requests for additional data should be directed to the lead contact.

### Materials and methods

See the Supplemental experimental procedures for full details of materials, characterization, and Metropolis non-negative matrix factorization.

## SUPPLEMENTAL INFORMATION

Supplemental information can be found online at https://doi.org/10.1016/j.xcrp.2021.100543.

## AUTHOR CONTRIBUTIONS

X.H. conceived the study. X.H. planned the project with help from P.K.A. and A.L.G. X.H. prepared the materials and analyzed the electrochemical data with help from P.K.A. and support from A.M., E.C.-M., and P.G.B. X.H. and P.K.A. carried out the *in situ* PDF experiments with help from P.A.C. X.H. performed NMF analysis with help from H.S.G., T.S.D., and A.L.G. The manuscript was written by X.H. and revised

by E.C.-M. and A.L.G. All authors contributed to discussions and commented on the manuscript.

## REFERENCES

1. Grey, C.P., and Hall, D.S. (2020). Prospects for lithium-ion batteries and beyond—a 2030 vision. Nat. Commun. *11*, 6279.

2. Cabana, J., Monconduit, L., Larcher, D., and Palacín, M.R. (2010). Beyond intercalation-based Li-ion batteries: the state of the art and challenges of electrode materials reacting through conversion reactions. Adv. Mater. *22*, E170–E192.

3. Nitta, N., Wu, F., Lee, J.T., and Yushin, G. (2015). Li-ion battery materials: present and future. Mater. Today *18*, 252–264.

4. Yu, S.-H., Lee, S.H., Lee, D.J., Sung, Y.-E., and Hyeon, T. (2016). Conversion Reaction-Based Oxide Nanomaterials for Lithium Ion Battery Anodes. Small *12*, 2146–2172.

5. Huang, Y., Xu, Z., Mai, J., Lau, T.-K., Lu, X., Hsu, Y.-J., Chen, Y., Lee, A.C., Hou, Y., Meng, Y.S., and Li, Q. (2017). Revisiting the origin of cycling enhanced capacity of Fe₃O₄ based nanostructured electrode for lithium ion batteries. Nano Energy *41*, 426–433.

6. Delmer, O., Balaya, P., Kienle, L., and Maier, J. (2008). Enhanced Potential of Amorphous Electrode Materials: Case Study of RuO₂. Adv. Mater. *20*, 501–505.

7. Hu, Y.-Y., Liu, Z., Nam, K.-W., Borkiewicz, O.J., Cheng, J., Hua, X., Dunstan, M.T., Yu, X., Wiaderek, K.M., Du, L.-S., et al. (2013). Origin of additional capacities in metal oxide lithium-ion battery electrodes. Nat. Mater. *12*, 1130–1136.

8. Li, Q., Li, H., Xia, Q., Hu, Z., Zhu, Y., Yan, S., Ge, C., Zhang, Q., Wang, X., Shang, X., et al. (2021). Extra storage capacity in transition metal oxide lithium-ion batteries revealed by *in situ* magnetometry. Nat. Mater. *20*, 76–83.

9. Ng, B., Faegh, E., Lateef, S., Karakalos, S.G., and Mustain, W.E. (2021). Structure and chemistry of the solid electrolyte interphase (SEI) on a high capacity conversion-based anode: NiO. J. Mater. Chem. A Mater. Energy Sustain. *9*, 523–537.

10. Ponrouch, A., Taberna, P.-L., Simon, P., and Palacín, M.R. (2012). On the origin of the extra capacity at low potential in materials for Li batteries reacting through conversion reaction. Electrochim. Acta *61*, 13–18.

11. Poizot, P., Laruelle, S., Grugeon, S., Dupont, L., and Tarascon, J.M. (2000). Nano-sized transition-metal oxides as negative-electrode materials for lithium-ion batteries. Nature *407*, 496–499.

12. Lowe, M.A., Gao, J., and Abruna, H.D. (2013). In operando X-ray studies of the conversion reaction in Mn₃O₄ lithium battery anodes. J. Mater. Chem. A Mater. Energy Sustain. *1*, 2094–2103.

13. Butala, M.M., Danks, K.R., Lumley, M.A., Zhou, S., Melot, B.C., and Seshadri, R. (2016). MnO Conversion in Li-Ion Batteries: *In Situ* Studies and the Role of Mesostructuring. ACS Appl. Mater. Interfaces *8*, 6496–6503.

14. Yonekura, D., Iwama, E., Ota, N., Muramatsu, M., Saito, M., Orikasa, Y., Naoi, W., and Naoi, K. (2014). Progress of the conversion reaction of Mn₃O₄ particles as a function of the depth of discharge. Phys. Chem. Chem. Phys. *16*, 6027–6032.

15. Zhang, W., Li, Y., Wu, L., Duan, Y., Kisslinger, K., Chen, C., Bock, D.C., Pan, F., Zhu, Y., Marschilok, A.C., et al. (2019). Multi-electron transfer enabled by topotactic reaction in magnetite. Nat. Commun. *10*, 1972.

16. Li, J., Hwang, S., Guo, F., Li, S., Chen, Z., Kou, R., Sun, K., Sun, C.-J., Gan, H., Yu, A., et al. (2019). Phase evolution of conversion-type electrode for lithium ion batteries. Nat. Commun. *10*, 2224.

17. Zhang, W., Bock, D.C., Pelliccione, C.J., Li, Y., Wu, L., Zhu, Y., Marschilok, A.C., Takeuchi, E.S., Takeuchi, K.J., and Wang, F. (2016). Insights into Ionic Transport and Structural Changes in Magnetite during Multiple-Electron Transfer Reactions. Adv. Energy Mater. *6*, 1502471.

18. Zhukovskii, Y.F., Balaya, P., Kotomin, E.A., and Maier, J. (2006). Evidence for interfacial-storage anomaly in nanocomposites for lithium batteries from first-principles simulations. Phys. Rev. Lett. *96*, 058302.

19. Billinge, S.J.L., and Levin, I. (2007). The problem with determining atomic structure at the nanoscale. Science *316*, 561–565.

20. Lee, D.D., and Seung, H.S. (1999). Learning the parts of objects by non-negative matrix factorization. Nature *401*, 788–791.

21. Geddes, H.S., Blade, H., McCabe, J.F., Hughes, L.P., and Goodwin, A.L. (2019). Structural characterisation of amorphous solid dispersions via metropolis matrix factorisation of pair distribution function data. Chem. Commun. (Camb.) *55*, 13346–13349.

22. Hua, X., Allan, P.K., Gong, C., Chater, P.A., Schmidt, E.M., Geddes, H.S., Robertson, A.W., Bruce, P.G., and Goodwin, A.L. (2021). Non-equilibrium metal oxides via reconversion chemistry in lithium-ion batteries. Nat. Commun. *12*, 561.

23. Thackeray, M.M., David, W.I.F., and Goodenough, J.B. (1982). Structural characterization of the lithiated iron oxides LiₓFe₃O₄ and LiₓFe₂O₃ (0 < x < 2). Mater. Res. Bull. *17*, 785–793.

24. Larcher, D., Masquelier, C., Bonnin, D., Chabre, Y., Masson, V., Leriche, J.-B., and Tarascon, J.-M. (2003). Effect of Particle Size on Lithium Intercalation into α-Fe₂O₃. J. Electrochem. Soc. *150*, A133–A139.

25. Bock, D.C., Pelliccione, C.J., Zhang, W., Timoshenko, J., Knehr, K.W., West, A.C., Wang, F., Li, Y., Frenkel, A.I., Takeuchi, E.S., et al. (2017). Size dependent behavior of Fe₃O₄ crystals during electrochemical (de)lithiation: an *in situ* X-ray diffraction, *ex situ* X-ray absorption spectroscopy, transmission electron microscopy and theoretical investigation. Phys. Chem. Chem. Phys. *19*, 20867–20880.

26. Shyam, B., Chapman, K.W., Balasubramanian, M., Klingler, R.J., Srajer, G., and Chupas, P.J. (2012). Structural and mechanistic revelations on an iron conversion reaction from pair distribution function analysis. Angew. Chem. Int. Ed. Engl. *51*, 4852–4855.

27. Jain, A., Ong, S.P., Hautier, G., Chen, W., Richards, W.D., Dacek, S., Cholia, S., Gunter, D., Skinner, D., Ceder, G., and Persson, K.A. (2013). Commentary: The Materials Project: A materials genome approach to accelerating materials innovation. APL Mater. *1*, 011002.

28. Larcher, D., Bonnin, D., Cortes, R., Rivals, I., Personnaz, L., and Tarascon, J.M. (2003). Combined XRD, EXAFS, and Mössbauer Studies of the Reduction by Lithium of α-Fe₂O₃ with Various Particle Sizes. J. Electrochem. Soc. *150*, A1643.

29. Bekaert, E., Balaya, P., Murugavel, S., Maier, J., and Ménétrier, M. (2009). 6Li MAS NMR Investigation of Electrochemical Lithiation of RuO₂: Evidence for an Interfacial Storage Mechanism. Chem. Mater. *21*, 856–861.

30. Howell, R., Proffen, T., and Conradson, S. (2006). Pair distribution function and structure factor of spherical particles. Phys. Rev. B Condens. Matter Mater. Phys. *73*, 094107.

31. He, K., Zhang, S., Li, J., Yu, X., Meng, Q., Zhu, Y., Hu, E., Sun, K., Yun, H., Yang, X.-Q., et al. (2016). Visualizing non-equilibrium lithiation of

spinel oxide via *in situ* transmission electron microscopy. Nat. Commun. *7*, 11441.

32. Thackeray, M.M., de Picciotto, L.A., de Kock, A., Johnson, P.J., Nicholas, V.A., and Adendorff, K.T. (1987). Spinel electrodes for lithium batteries—A review. J. Power Sources *21*, 1–8.

33. Clément, R.J., Lun, Z., and Ceder, G. (2020). Cation-disordered rocksalt transition metal oxides and oxyfluorides for high energy lithium-ion cathodes. Energy Environ. Sci. *13*, 345–373.

34. House, R.A., Jin, L., Maitra, U., Tsuruta, K., Somerville, J.W., Förstermann, D.P., Massel, F., Duda, L., Roberts, M.R., and Bruce, P.G. (2018). Lithium manganese oxyfluoride as a new cathode material exhibiting oxygen redox. Energy Environ. Sci. *11*, 926–932.

35. Liu, H., Zhu, Z., Yan, Q., Yu, S., He, X., Chen, Y., Zhang, R., Ma, L., Liu, T., Li, M., et al. (2020). A disordered rock salt anode for fast-charging lithium-ion batteries. Nature *585*, 63–67.

36. Lun, Z., Ouyang, B., Kwon, D.-H., Ha, Y., Foley, E.E., Huang, T.-Y., Cai, Z., Kim, H., Balasubramanian, M., Sun, Y., et al. (2021). Cation-disordered rocksalt-type high-entropy

cathodes for Li-ion batteries. Nat. Mater. *20*, 214–221.

37. Chapman, K.W., Lapidus, S.H., and Chupas, P.J. (2015). Applications of principal component analysis to pair distribution function data. J. Appl. Cryst. *48*, 1619–1626.

38. Chen, S., Sheikh, A.Y., and Ho, R. (2014). Evaluation of effects of pharmaceutical processing on structural disorders of active pharmaceutical ingredient crystals using nanoindentation and high-resolution total scattering pair distribution function analysis. J. Pharm. Sci. *103*, 3879–3890.

39. Cole, J.M., Cheng, X., and Payne, M.C. (2016). Modeling Pair Distribution Functions of Rare-Earth Phosphate Glasses Using Principal Component Analysis. Inorg. Chem. *55*, 10870–10880.

40. Li, W., Borkiewicz, O.J., Saubanère, M., Doublet, M.-L., Flahaut, D., Chupas, P.J., Chapman, K.W., and Dambournet, D. (2018). Atomic Structure of 2 nm Size Metallic Cobalt Prepared by Electrochemical Conversion: An *in Situ* Pair Distribution Function Study. J. Phys. Chem. C *122*, 23861–23866.

41. Hua, X., Eggeman, A.S., Castillo-Martínez, E., Robert, R., Geddes, H.S., Lu, Z., Pickard, C.J., Meng, W., Wiaderek, K.M., Pereira, N., et al. (2021). Revisiting metal fluorides as lithium-ion battery cathodes. Nat. Mater. *20*, 841–850.

42. Gambardella, A.A., Cotte, M., de Nolf, W., Schnetz, K., Erdmann, R., van Elsas, R., Gonzalez, V., Wallert, A., Iedema, P.D., Eveno, M., and Keune, K. (2020). Sulfur K-edge micro- and full-field XANES identify marker for preparation method of ultramarine pigment from lapis lazuli in historical paints. Sci. Adv. *6*, eaay8782.

43. Tanimoto, H., Hongkun, X., Mizumaki, M., Seno, Y., Kimura, Y., Amezawa, K., Akai, I., and Aonishi, T. (2020). Non-Negative Matrix Factorization for 2D-XAS Images of Lithium Ion Batteries. arXiv e-prints, arXiv, 2009.02873.

44. Sapnik, A.F., Geddes, H.S., Reynolds, E.M., Yeung, H.H.M., and Goodwin, A.L. (2018). Compositional inhomogeneity and tuneable thermal expansion in mixed-metal ZIF-8 analogues. Chem. Commun. (Camb.) *54*, 9651–9654.